Ultrasound in Med. & Biol., Vol. 35, No. 1, pp. 79–93, 2009

0301-5629/09/$–see front matter

doi:10.1016/j.ultrasmedbio.2008.07.004

● *Original Contribution*

A REAL-TIME FREEHAND ULTRASOUND CALIBRATION SYSTEM WITH AUTOMATIC ACCURACY FEEDBACK AND CONTROL

THOMAS KUIRAN CHEN* ADRIAN D. THURSTON,* RANDY E. ELLIS,*[‡] and PURANG ABOLMAESUMI,*[†]

*School of Computing, Queen's University, Kingston, Canada; [†]Department of Electrical and Computer Engineering, Queen's University, Kingson, Canada; and [‡]Division of Orthopaedic Surgery, Kingston General Hospital, Kingston, Canada

(*Recieved* 6 *November* 2007; *revised* 16 *April* 2008; *in final form* 15 *July* 2008)

Abstract—This article describes a fully automatic, real-time, freehand ultrasound calibration system. The system was designed to be simple and sterilizable, intended for operating-room usage. The calibration system employed an automatic-error-retrieval and accuracy-control mechanism based on a set of ground-truth data. Extensive validations were conducted on a data set of 10,000 images in 50 independent calibration trials to thoroughly investigate the accuracy, robustness, and performance of the calibration system. On average, the calibration accuracy (measured in three-dimensional reconstruction error against a known ground truth) of all 50 trials was 0.66 mm. In addition, the calibration errors converged to submillimeter in 98% of all trials within 12.5 s on average. Overall, the calibration system was able to consistently, efficiently and robustly achieve high calibration accuracy with real-time performance. (E-mail: purang@cs.queensu.ca) **© 2008 World Federation for Ultrasound in Medicine & Biology.**

Key Words: **Freehand ultrasound imaging, Real-time calibration, Automatic error retrieval, Real-time accuracy control, *Double-N* phantom, Computer-assisted surgery.**

INTRODUCTION

Three-dimensional (3D) ultrasound imaging has seen increasing applications in intraoperative guidance of computer-assisted surgery. Medical ultrasound is non-ionizing, compact, portable, relatively inexpensive and capable of imaging in real time. To construct a high-resolution 3D ultrasound image of the patient's anatomy from a set of two-dimensional (2D) images, a tracked 2D ultrasound probe that allows image acquisition in an unconstrained "freehand" motion is commonly used. Tracking is typically achieved by rigidly affixing the probe with a localizer traced by a position sensing system. However, knowing the position of the ultrasound probe alone is not adequate to determine the positions of the acquired 2D images. The relationship between these two coordinate frames can be calculated through the process of ultrasound probe calibration, where a homogeneous transformation is estimated to map the position of individual pixels from the ultrasound image frame to the ultrasound probe frame. With the latter being tracked in real time by the tracking system, we are able to obtain the physical positions of those pixels in the world coordinate frame, which is normally fixed to the imaging anatomy. Calibration is, therefore, a fundamental step and a single point of failure in a freehand ultrasound imaging system.

The calibration procedure is typically conducted by imaging an artificial object with known geometries, referred to as a phantom. Widely used calibration phantoms include the single-point or cross-wire phantoms (Barry et al. 1997; Prager et al. 1998; Muratore and Galloway Jr. 2001), the three-wire phantom (Prager et al. 1998), the single-wall and Cambridge phantoms (Prager et al. 1998), the Hopkins phantom (Boctor et al. 2003), the Z-fiducial or N-wire phantoms (Pagoulatos et al. 2001; Lindseth et al. 2003; Zhang et al. 2004; Chen et al. 2005; Hsu et al. 2007), and the Sandwich phantom (Boctor et al. 2006a). Recently, phantomless (also referred to as self-calibrating) calibration techniques were also proposed (Barratt et al. 2006; Boctor et al. 2006b), where images from actual patient were used instead of a specific calibration phantom. A recent and comprehen-

Address correspondence to: Purang Abolmaesumi, School of Computing, Queen's University, Kingston, Ontario, Canada K7L 3N6. E-mail: purang@cs.queensu.ca

sive overview of the ultrasound calibration techniques may be found in Mercier et al. (2005). Most of the state-of-the-art calibration techniques focus primarily on precision and accuracy, for which sound repeatability and up to submillimeter accuracy can be achieved (Mercier et al. 2005); however, for computer-assisted surgeries that may require calibration inside an operating room (OR), many other aspects must be considered.

First, intraoperative use needs a calibration procedure that is fast, robust and easy to perform. Overall, calibration techniques may be divided into (Mercier et al. 2005) either an iterative approach (*e.g.,* single-point or cross-wire phantoms, three-wire phantoms, and wall phantoms) or a closed-form solution (*e.g.,* N-wire phantoms and the Sandwich phantom). Iterative approaches are, in general, less robust than closed-formed solutions because of the nonguaranteed convergence, local minima and sensitiveness to initial estimates (Eggert et al. 1997). Also, to achieve a similar accuracy, iterative methods typically need more input data and computational time than closed-form techniques. For instance, calibration with the Cambridge phantom (Prager et al. 1998) would require at least 550 images to achieve acceptable accuracy, compared with around 6 to 30 images with a typical N-wire phantom (Pagoulatos et al. 2001; Lindseth et al. 2003; Zhang et al. 2004; Chen et al. 2005; Hsu et al. 2007). On the other hand, closed-form solutions face the challenge to automatically and accurately extract point-targets from an ultrasound image and are, therefore, typically conducted manually, which is undesirable in an OR set-up. Some successful attempts have been made by Lindseth et al. (2003) and Hsu et al. (2007) to automate segmentation on images acquired from N-wire phantoms, but their approaches all require human interferences to certain extent: *i.e.,* the former requires finding an image point in a manually specified region as an initialization of the algorithm and the latter needs to know the actual scale factors of the ultrasound image which have to be manually measured on the ultrasound machine.

Second, it is desirable to have automatic, real-time feedback of calibration accuracy in the OR. Calibration and validation are conventionally two-phase tasks that are isolated: a calibration is performed, followed by a validation, so the only way for a surgeon to improve an inaccurate calibration is to recalibrate (which is not only time-consuming but lacks an inherent accuracy check). Boctor et al. were among the first to introduce a real-time *in vivo* quality control mechanism that monitored the consistency in calibration parameters through frequent recalibration in the background (Boctor et al. 2005, 2006b). However, their validation on the calibration results was based on precision and not accuracy. It is important to note that a measure of precision is quite different from that of accuracy (Mercier et al. 2005): precision defines the repeatability and consistency of the system, while accuracy evaluates how much the output is away from a known "ground truth" (typically measured independently). Not relying on a ground truth, a high precision (a low variance in results) does not necessarily guarantee a high accuracy. For example, it is possible that a calibration system that achieves highly consistent results may include a systematic error that renders the system inaccurate.

Another major concern in OR usage is sterilization of the calibration phantom and easy assembly. Most of the current phantom designs are in general complicated and not optimized for such procedure.

To the best of our knowledge, state-of-the-art calibration techniques in the literature (Mercier et al. 2005; Chen et al. 2005; Barratt et al. 2006; Boctor et al. 2006a; Boctor et al. 2006b; Hsu et al. 2007) have yet to address all of the aforementioned concerns altogether. Our research goal was to address all these concerns in a practical calibration solution intended for operating-room usage. We designed and tested a real-time ultrasound calibration system that needed minimal human interaction and was equipped with automatic error retrieval and accuracy control based on a known ground truth. Extensive validations were conducted on a data set of 10,000 images in 50 independent calibration trials to thoroughly investigate the accuracy, robustness and performance of the calibration system. In our tests, the system was able to consistently achieve submillimeter calibration accuracy while providing feedback on the error convergency in real time. On average, the calibration accuracy (measured in 3D reconstruction error against a known ground truth) of all 50 trials was 0.66 mm. In addition, the calibration errors converged to submillimeter in 98% of all trials within 12.5 s on average. An important part of the system was a *Double-N* calibration phantom of a simple, sterilizable design.

The remainder of this article is organized as follows. First, an overview of the system design is given. Then, the design and specifications of the *Double-N* calibration phantom are presented, along with an in-depth analysis of how the ultrasound resolution would play a major role in our selection of N-wires. Then, our experimental set-ups in image acquisition and position tracking, as well as the coupling mechanism between these two processes are introduced. Further, the robust and fully automatic segmentation algorithm is explored step by step. We then discuss the details of our closed-form calibration solution, and illustrate the automatic error retrieval and real-time accuracy control for the calibration system. Finally, extensive validation results are demonstrated, followed by our detailed discussions and the conclusions.

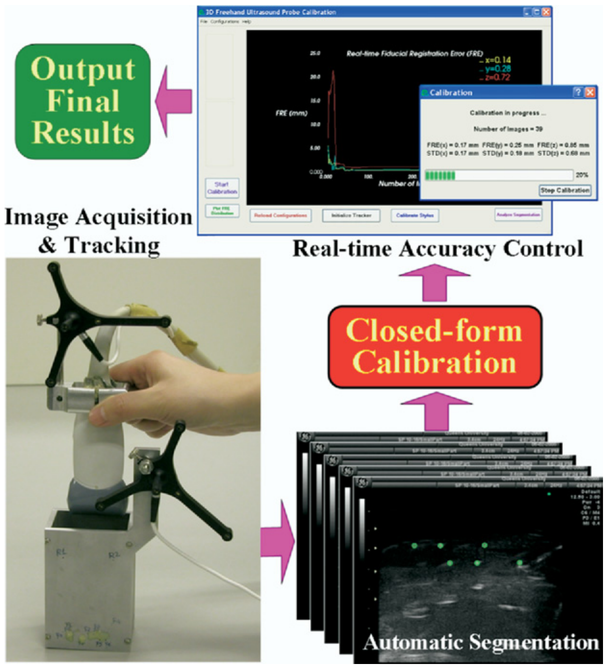

Fig. 1. The design of the real-time automatic ultrasound calibration system. Ultrasound images are acquired from *Double-N* calibration phantom and tracked in real time; N-wire pixel locations are then automatically extracted by the segmentation algorithm; Segmented points and their corresponding physical coordinates in the phantom are fed to a closed-form method to obtain the calibration parameters; Measured in fiducial registration error (FRE) and displayed in real time to the user, the calibration accuracy is fed back to the control loop to determine if it is satisfactory; Once FRE converges or reaches satisfaction, an interface is provided to the user to stop the process and output the calibration result.

METHODS AND MATERIALS

System overview

This section presents a high-level overview of our proposed ultrasound calibration system, along with a description of its hardware set-up.

Design of the real-time automatic calibration system. Figure 1 shows the design of our calibration system consisting five successive stages.

(1) Serving as input, ultrasound images were continuously acquired from the *Double-N* phantom. The position of the ultrasound probe was tracked by a camera system.
(2) The pixel locations of the cross section of N-wires in the ultrasound images (denoted as N-fiducials) were then extracted in real time by a fully automatic segmentation algorithm.
(3) The successfully segmented N-fiducials, together with their corresponding physical coordinates collected in the phantom space, were fed to a closed-form formula to calculate the calibration parameters.
(4) Measured by fiducial registration error (FRE) against a known ground truth, the accuracy of the current calibration result was fed back to the control loop to determine whether or not it was satisfactory. The FREs were updated, monitored and displayed in real time to the user.
(5) Once FRE converged or reached an acceptable level, an interactive interface was provided to the user to terminate the process and save the calibration result.

Hardware configurations. Figure 2 shows our hardware configuration for the automatic real-time calibration system:

- Images were generated by a ultrasound machine (Voluson 730 Expert, General Electric Canada, Mississauga, ON, Canada), shown in Fig. 2a-right, then fed to a frame grabber (ATI All-In-Wonder 7500, ATI Technologies Inc., Markham, ON, Canada).
- The ultrasound probe used in our experiments was a 192-element linear-array transducer (SP10–16 Wide Band, General Electric Canada, Mississauga, ON, Canada) that operated at a central frequency of 12.5MHz with imaging depth of 3.4 cm and 4 focal zones activated (Fig. 2c). The frame rate for image acquisition was 24 Hz.
- A four-marker optical target (VersaTrax Active Tracker, Traxtal Inc., Toronto, ON, Canada) was mounted on the ultrasound probe and tracked in real time by a camera (Optotrak Certus Optical Tracking System, Northern Digital Inc., Waterloo, ON, Canada), shown by Fig. 2a-left. The camera employed three sensors (Fig. 2b) to track infrared signals emitted by the optical targets, and had a root-mean-square (RMS) accuracy of 0.1 mm in X and Y axes, and 0.15 mm in Z-axis, all measured at a stand-off distance of 2.25 m (Northern Digital Inc.).
- The central processor was a desktop workstation (Dell Optiplex GX270, Dell Canada, North York, ON, Canada) with a Intel Pentium 4 2.6GHz CPU and 2GB SDRAM running Microsoft Windows XP Professional.

Software system design and specifications. From a software-architecture point of view, the calibration system was designed and developed using a multiple-component-based object-oriented methodology. It encompassed four essential system components: ultrasound image acquisition and tracking, automatic segmentation, closed-form calibration, and real-time accuracy feedback and control. A number of open-source frameworks were employed, including the Visualization Toolkit (VTK), QT framework, Vision Numerics Library (VNL) and Microsoft DirectShow. Figure 3 demonstrates the high-level component-based system design and implementa-

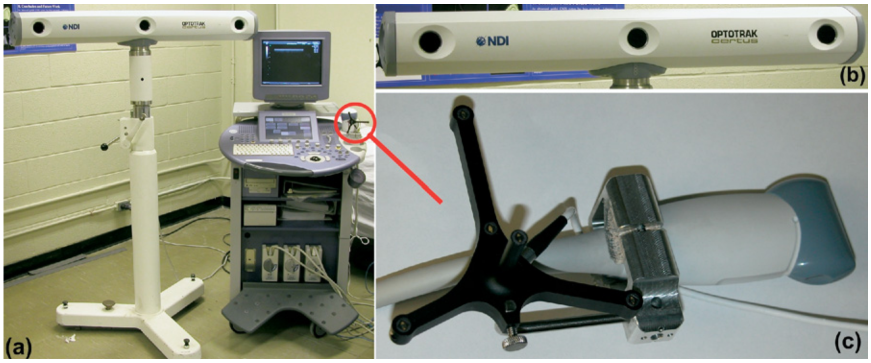

Fig. 2. Hardware configuration for image acquisition and tracking. Images were generated by a GE Voluson 730 Expert ultrasound machine (a-right). The ultrasound probe was a 192-element GE SP10–16 wide band linear-array transducer operating at a central frequency of 12.5 MHz, with imaging depth of 3.4 cm and four focal zones activated (c). The image-acquisition frame rate was set at 24 Hz. A four-marker Traxtal VersaTrax Active Tracker was mounted on the ultrasound probe (red circle in a-right) and tracked in real time by a NDI Optotrak Certus Optical Tracking System (a-left) which employed three infrared sensors (b).

tion in unified modeling language (UML) (Booch et al. 1998).

The Double-N calibration phantom

Material and constructions. The *Double-N* phantom consisted of a front and a back plate connected by two side walls, forming a simple open-ended box and measured as 105 $mm \times 70\ mm \times 50\ mm$ in dimensions (Fig. 4). For effective sterilization, the phantom could be quickly disassembled and reassembled using an L-Key screwdriver. To facilitate easy manufacture, ensure rigidity and durability and reduce distortion in the phantom geometry during the reassembling procedure, the plates were designed in plain rectangle-shape and made of 5 mm-thick aluminum. There were six holes on both the front and back plate to mount the upper and lower layers of N-wires that were 10 mm apart. Each set of N-wires was 20 mm wide (measured as the distance between the two parallel wires), which best accommodated the size of the ultrasound transducer in use. The ends of nylon wires were affixed using silicon glue which not only ensured sufficient tension of the wires but was also quickly detachable (when heated) for easy sterilization. The front plate had an extended arm to mount a spatial localizer for tracking purposes.

Selection of nylon wires. The typical cross-sectional appearance of a nylon wire in a ultrasound image is a small dot. Two important acoustic features make nylon an ideal candidate for N-wires:

- It has an acoustic impedance (2.9 M rayl) that is roughly that of distilled water (1.48 M rayl) and, as a result, a reflection coefficient of 0.32; this makes nylon an acceptable sound-reflective material in water.
- Nylon can be manufactured at a diameter comparable to ultrasound wavelengths, which are typically less than 0.5 mm for medical ultrasound (Hedrick et al. 2005), resulting in small but well-defined dots in the image.

We found that the image appearance of the nylon wire is largely determined by the axial and lateral resolutions in the ultrasound scan plane (Hedrick et al. 2005). The axial resolution in ultrasound imaging is the minimum separation (distance) of two objects along the axial axis that could be distinguished by two separate echoes; it also determines the smallest object detectable by the sound wave in its direction of propagation. In theory, the axial resolution is equal to half the spatial pulse length (or SPL), which is the product of the ultrasound wavelength and the number of cycles. Because the number of cycles is typically fixed by the transducer design, the axial resolution is proportional to the sound wavelength and is independent of the image depth. In general, the higher the operational frequency of the transducer, the smaller the wave length and the better the axial resolution. For our broadband linear-array transducer operating at a central frequency of 12.5 MHz, the axial resolution was approximately 0.1 mm; thus, any object of a dimension greater than 0.1 mm along the axial direction should be resolvable by the sound wave. Figure 5 shows our experiment of imaging a nylon wire at 0.203 mm diameter across different image depths (the pixel resolution of the ultrasound image is 0.1 mm/pixel). Because the diameter of the nylon wire was greater than the axial resolution, the axial height of the wire was correctly represented in the image and remained the same at various depths as the axial resolution did not change with depth.

Similarly, the lateral resolution defines the ability to

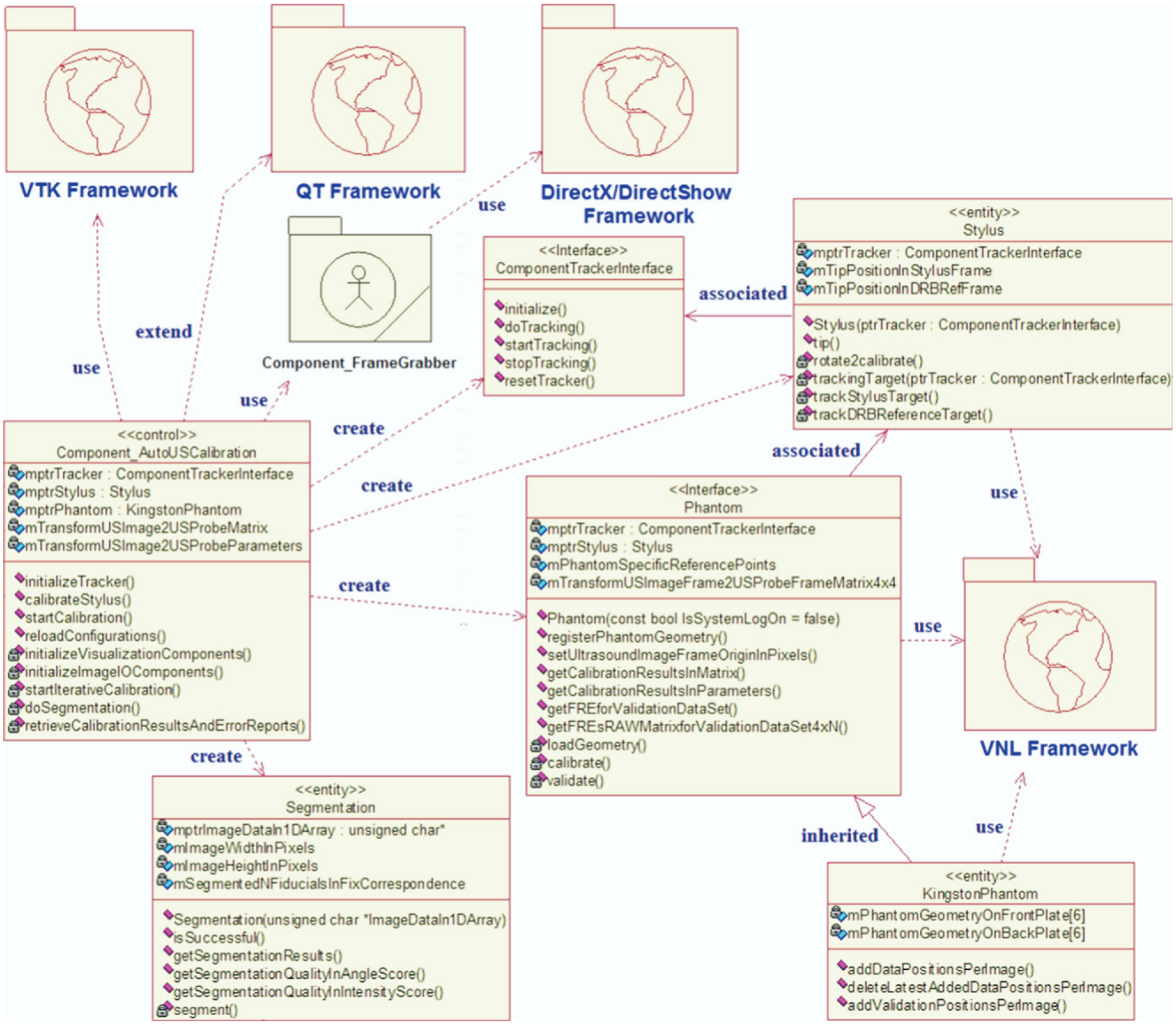

Fig. 3. A high level object-oriented design graph of the calibration system in industry-standard unified modeling language (UML). The calibration software system contains four essential components: ultrasound image acquisition and tracking, automatic segmentation, closed-form calibration, and real-time accuracy feedback and control. A number of open-source frameworks were employed, including the Visualization Toolkit (VTK), QT framework, Vision Numerics Library (VNL) and Microsoft DirectShow.

tell apart two objects located side-by-side in the lateral direction (perpendicular to the sound propagation in the scan plane). Unlike the axial resolution, lateral resolution is determined by ultrasound lateral beam width and varies with the axial depth (Kremkau 2002). For a linear crystal array, the multiple-element transducer electronically focused and swept the ultrasound beam in the field of view by sequentially firing the crystals in groups. The sound beam had a finite width laterally so, if an object was smaller than the beam width, the object would reflect numerous echoes back to the transducer as the sound beam swept across it; this registered a short line-alike shape in the display, with the length of the line directly proportional to the lateral beam width at that image depth. Therefore, because of the lateral beam width, point-shaped small objects were misrepresented and appeared as short lines in the image. This phenomenon is evident in Fig. 5, which shows the sonographic cross-sections of a nylon wire at various depths. As can readily be seen, the ideal circle-shaped cross-section of the nylon wire is distorted (except when at the focal depth).

The diameter of the nylon wire also has a significant effect on imaging. We compared the overall influence of both axial and lateral resolutions on nylon wires at different diameters, ranging from 0.203 mm up to 0.457 mm, all at the scan-plane focal depth (Fig.

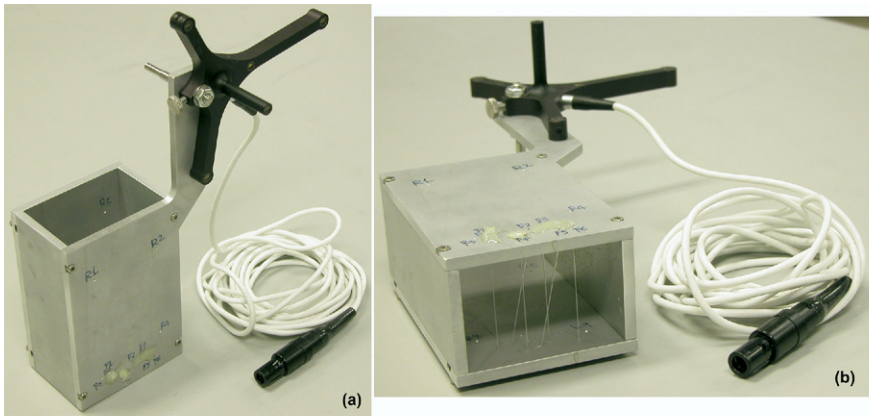

Fig. 4. Front and side views of the *Double-N* phantom. The phantom consists of only a front and a back plate plus two side walls to form a simple cubic pipe, measured as 105 mm × 70 mm × 50 mm in dimensions. The plates are designed in plain rectangle-shape and made of stainless steel at 5 mm thickness. The front plate has an extended arm to mount a spatial localizer for tracking purposes.

6). For our broadband transducer operating at a central frequency of 12.5 MHz (with a wavelength around 0.1 mm), we selected the nylon wire of 0.356 mm diameter as having the best overall definition (most circular) in both axial and lateral axes. Note that the choice of diameter may vary when another transducer with different operational frequency (wavelength) is used. We found in our experiments that the general rule of thumb is to use wire of diameter that is slightly larger than the operational ultrasound wavelength, then to choose a wire with the lateral width (at the image plane focal point) closest to the axial height in its image appearance (or in other words, the dot appears to be more circular in shape).

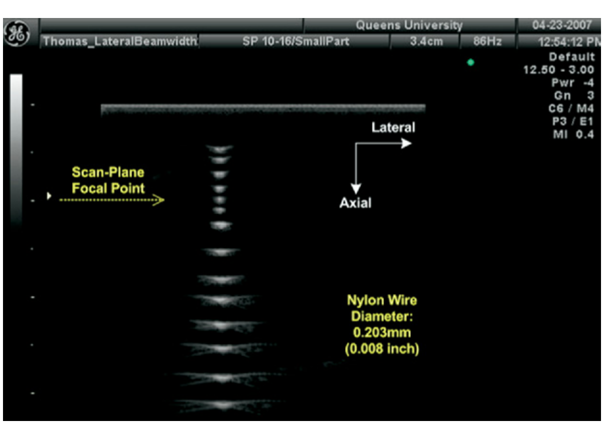

Fig. 5. Wire appearance determined by the ultrasound axial and lateral resolutions. The axial height of the dot is determined by the axial resolution which does not change with the image depth. The lateral width of the dot is directly proportional to the lateral resolution (the lateral beam width) at that depth and is depth-dependent.

Phantom design. Figure 7 illustrates the design of the *Double-N* phantom. There are only two layers of N-wires, shifted horizontally to improve imaging and reduce the occurrence of reverberance artifacts that may arise if more than two layers are used (Chen 2005). With the nylon wire selected by empirically imaging various diameters, the *Double-N* phantom produced remarkably clean and well defined ultrasound images of N-fiducials that facilitated automated segmentation.

Image acquisition and position tracking

Experimental set-up for image acquisition and tracking. Ultrasound images were acquired from the *Double-N* calibration phantom in a clean-water bath. Both the transducer and the phantom were rigidly affixed with optical targets and tracked in real time by the camera system. To approximate the speed of sound in tissue (1540 m/s), the water temperature was raised up to 37° C, in which sound travels at about 1570 m/s (Hedrick et al. 2005). The ultrasound transducer was held freehand such that the acquired image would display the cross-section of the N-wires.

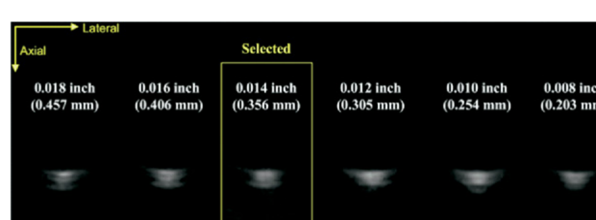

Fig. 6. Appearance of nylon wires of different diameters at the ultrasound scan-plane focal depth. The 0.356 mm wire gives the best (most circular) image definition.

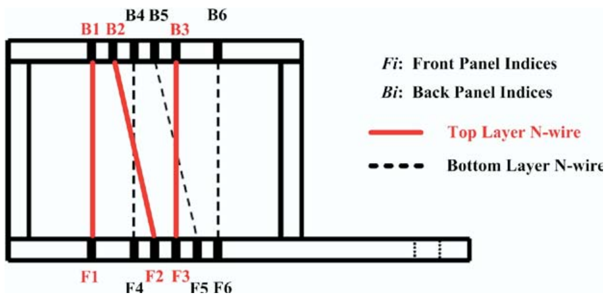

Fig. 7. Design specifications of the *Double-N* phantom. The phantom is 105 mm × 70 mm × 50 mm in dimensions. There are six holes on both the front and back plate to mount the upper and lower layers of N-wires that are 10 mm apart. Each set of N-wires is 20 mm wide (measured as the distance between the two parallel wires), which best accommodates the size of the ultrasound transducer in use.

Position tracking coupled with image acquisition. Image acquisition and position tracking were performed with distinct hardware that were closely coupled by assigning position data to each captured image.

(1) The program was triggered by the image acquisition component when a new image was updated to its buffer; it would then attempt to read the position of the tracked ultrasound probe from the tracking component.
(2) If that attempt failed, the program would discard the image and go back to step-1 to wait for a new image. This procedure was repeated until the position data were successfully retrieved.
(3) The system stored both the image and the position data, ready for the next acquisition.

As a result, an image was always tagged with data that recorded the positions of the optical targets affixed to the ultrasound probe and the *Double-N* phantom. Along with the image, these positions served as inputs to the calibration pipeline.

Fast, robust, fully automatic segmentation

This section details the ultrasound image segmentation method we developed to robustly extract the N-fiducials.

The uniqueness in N-fiducial geometry. The typical appearance of an N-fiducial is a single small dot in the ultrasound image, which is challenging for automatic segmentation (opposed to a line object, which is easier to segment and is the basis of wall-phantom-based calibration techniques (Mercier et al. 2005)). A major difficulty is how to accurately and robustly recognize the N-fiducials in the presence of speckle, which has similar image intensities and shapes. The basic idea was to utilize two unique geometric features of N-fiducials in the image to assist the segmentation:

- the three collinear dots that form a typical N-wire intersection with the ultrasound image plane and
- the two nearly parallel lines that pass through these two layers of dots.

The automated segmentation algorithm. Our segmentation algorithm had four major stages involving various image processing techniques.

Stage 1. Morphological operations. Two morphological operations (Gonzalez and Woods 2002) were sequentially applied to remove speckles in the ultrasound image (Fig. 8a). The first removed any objects that were too big to represent an N-fiducial, which effectively eliminated large speckles. The morphological structural element used here was a bar of 1 pixel high and 18 pixels wide. The image was first eroded then dilated with this structural element. The result was then subtracted from the original image. The combination of erosion and then dilation is commonly referred to as an opening operation in image processing (Gonzalez and Woods 2002). This opening operation was applied three more times with the structural element rotated 45, 90 and 135 degrees clockwise, respectively, which removed large speckles along these orientations. Theoretically, more orientations could be used but in practice we found the above was sufficient to remove large noise while preserving the dots (N-fiducials) of our interest. The results of the first morphological operation are shown in Fig 8b. Take a note that the large speckles presented in the original image were gone, left alone the small speckles in the background.

The second operator removed speckles that were too small to be N-fiducials. We have found, through our experiments with nylon wires at various diameters, that the N-fiducials in the image have a minimal diameter of at least 6 pixels (with an imaging resolution of 0.1 mm/pixel). Therefore, here the morphological structural element was a circle at 2-pixel radius (or 0.4 mm in physical diameters) to effectively eliminate speckles that are smaller than that size, while making the remaining dots more uniform in shape. Similar to the first operation, an opening operation was applied with the morphological operation at four different orientations. After the second morphological operation, any remaining speckles in the resultant image were of a similar size to N-fiducials (Fig. 8c).

Stage 2. Pixel clustering. The image pixels were clustered to precisely identify the circle-shaped dots. The algorithm iterated through the image looking for a set (cluster) of pixels with similar intensities and then explored the neighbouring pixels looking for more alike pixels. The search continued until all pixels in the image have been accounted for or a black boundary is reached. Afterwards, a dot location was computed by combing the locations of all the clustered pixels that composed the dot

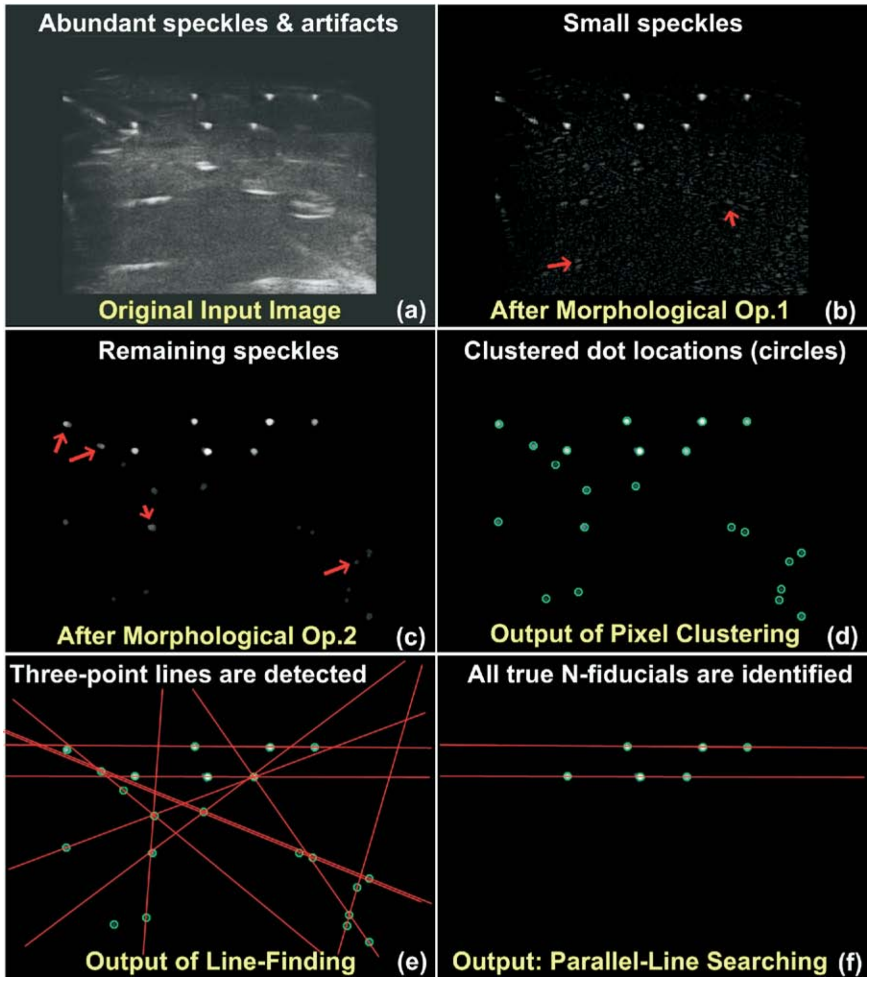

Fig. 8. Results of the fully automatic segmentation algorithm. (a) Original ultrasound image with exemplified poor visibility and abundance of speckles and noises; (b) Results of the first morphological operation which removed speckles larger than N-fiducials; (c) Results of the second morphological operation that removed speckles smaller than N-fiducials; (d) Output of the pixel clustering where the dot locations were identified (in green circles); (e) Results of the line finding that discovered sets of lines (in red lines) passing through three identified dots; (f) The final segmentation results after parallel-line searching where the two lines passing through the true N-fiducials were correctly extracted. The green circle indicated the segmented positions of the N-fiducials.

and then, scoring the pixels with a linear sum of their intensities. This approach effectively drove both the size and image intensity of a dot to influence its score, a measure that would find its use in the later line-finding stage. Upon completion, all dots would be properly segmented and scored. Keep in mind that the identified dots here included not only the desired N-fiducials, but also similarly shaped and sized speckles (Fig. 8d).

Stage-3. Line discovering. At this stage, we began to harness the special geometric relationships between the N-fiducials: we searched for sets of three dots that were collinear. Possible candidates were those segmented and scored dot locations from the clustering stage. A set of three distinct dots were accepted for further processing if the error in drawing a line through them was among the smallest in the overall ranking. Nevertheless, it would be unnecessary and inefficient to comb through all the candidates given the observation that majority of the segmented dots were those remaining speckles with typically lower intensity and smaller size than the N-fiducials. Hence, to speed up the search, we only processed and discovered those individual lines (drawn in red) passing through sets of three segmented dots that were higher ranked during pixel clustering (Fig. 8e).

Stage-4. Parallel-line searching. Finally, we located a pair of detected lines that were parallel to each other-the second unique relationship between N-fiducials. The simplest way to do that was to discard any pair of lines with an orientation difference that was greater

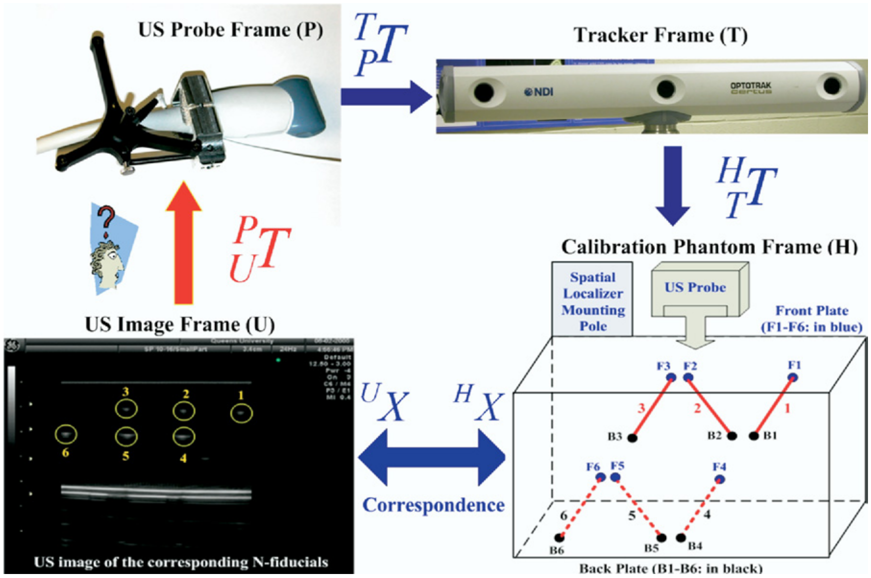

Fig. 9. Frame transformations to solve for calibration parameters. The geometry of *Double-N* calibration phantom helps to bridge the segmented points in the ultrasound image frame with their physical positions in the phantom space, through which a closed-form equation could be established.

than a small threshold. In our experiments, we chose an acceptable angle difference to be less than 2 degrees, which has proven to be more than sufficient in getting rid of the outliers. As a final result of segmentation, the two lines passing through the true N-fiducials were all correctly identified, as in Fig. 8f.

The closed-form calibration method

A closed-form solution for calibration parameters. A closed-form solution is any formula that can be evaluated using a fixed number of standard operations. In the case of calibration, the unique N-wire geometry of the *Double-N* phantom provided a series of 3D spatial frame transformations, from which we solved for the calibration parameters in a single closed-form equation (Fig. 9).

Let ${}^AX$ and ${}^BX$ denote a 3D position X expressed in coordinate frame A and B, respectively. ${}^B_AT$ then represents a homogeneous transform (Sciavicco and Siciliano 2000) that maps ${}^AX$ to ${}^BX$, as in:

$$ {}^BX = {}^B_AT \cdot {}^AX \tag{1} $$

The sole objective of a ultrasound probe calibration is to determine ${}^P_UT$, the homogeneous transform that brings a position from the ultrasound image frame (U), to the ultrasound probe frame (P). To start, we acquired a set of 2D ultrasound images from the *Double-N* phantom. The intersection point of a wire and the ultrasound image plane would display a gray-intensity dot in the image, which could be expressed in both the ultrasound image frame (U) and the *Double-N* phantom frame (H) as ${}^UX$ and ${}^HX$, respectively. From Fig. 9,

$$ {}^HX = {}^H_TT \cdot {}^T_PT \cdot {}^P_UT \cdot {}^UX \tag{2} $$

For nonsingular homogeneous transforms, $({}^B_AT)^{-1} = {}^A_BT$, so eqn 2 is equivalent to

$$ {}^P_UT \cdot {}^UX = {}^P_TT \cdot {}^T_HT \cdot {}^HX \tag{3} $$

On the right side of the eqn 3, ${}^P_TT$, the transform from the tracker frame to the ultrasound probe frame, was known from the optical target mounted on the probe. ${}^T_HT$, the transform from the phantom frame to the tracker frame, could be obtained by registering the *Double-N* phantom geometry to the optical target affixed to the phantom. On the left side, ${}^UX$ could be measured as the N-fiducial positions in the ultrasound image frame. Hence, if we could locate ${}^HX$, ${}^UX$'s corresponding positions in the *Double-N* phantom frame, we could solve for ${}^P_UT$ using a least-mean-square method. To find ${}^HX$, we utilized the *Double-N* phantom's unique N-wire geometry.

Finding ${}^{\mathrm{H}}\mathrm{X}$ *using the unique N-wire geometry.* Locating ${}^HX$ given ${}^UX$ can be done by using the distinctive N-wire geometry of the *Double-N* phantom. The fundamental principle was originally introduced by Brown (1979) to construct a stereotactic head frame for use with computed tomographic (CT) scans to provide guidance in neurosurgeries. It was later applied to closed-form ultrasound calibration by Comeau et al. (1998) and Pagoulatos et al. (1999).

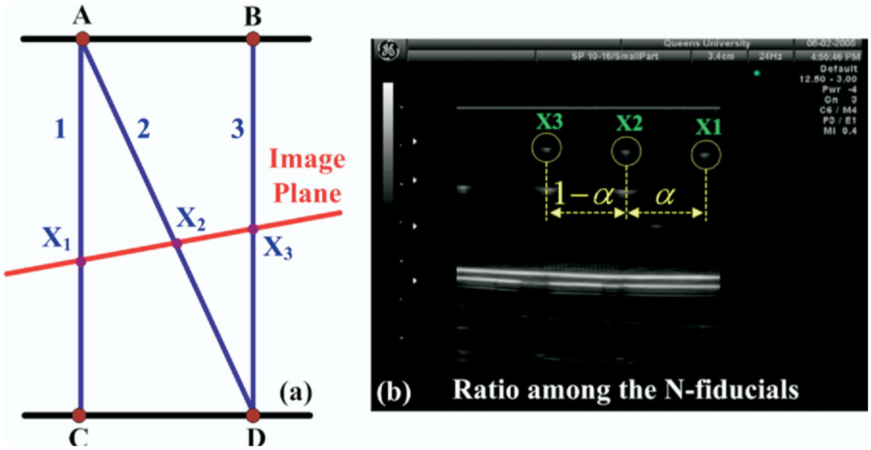

Fig. 10. Calculation of α-ratio based on the N-wire geometry. (a) The top view of the N-wires intersected by the ultrasound image plane; (b) The same intersection points are also revealed in the ultrasound image where the ratio, α, could be calculated.

When a ultrasound image was acquired from the N-wire phantom in a clean-water bath, both the ultrasound transducer and the phantom were oriented in such that the resultant image would show the cross-section of the wires. For the *Double-N* phantom (Fig. 9), there were six wires (labeled 1 to 6) that corresponded to six N-fiducials in the image, comprising two sets of N-wires (denoted as NW_{1-3} & NW_{4-6}).

To illustrate, consider NW_{1-3}, where the ultrasound image plane intersects the wires 1, 2 and 3 at position X_1, X_2 and X_3, respectively (Fig. 10a), producing three bright corresponding dots in the ultrasound image (Fig. 10b).

Because the *Double-N* phantom's front and back plates (*AB* and *CD* in Fig. 10a) were parallel to each other, the ratio α between the designated line segments is a consequence of the similar triangles fromed by the N-wires:

$$\alpha = \frac{\|A - X_2\|}{\|A - D\|} = \frac{\|X_1 - X_2\|}{\|X_1 - X_3\|} \tag{4}$$

where the form $\|P_i - P_j\|$ represents the Euclidean distance between two points P_i and P_j. The position X_2 in the phantom frame (H) can be calculated as

$${}^{H}X_2 = {}^{H}A + \alpha \cdot \left({}^{H}D - {}^{H}A\right) \tag{5}$$

Bear in mind that the same set of points (X_1, X_2 and X_3) also appear in the ultrasound image, albeit in a different coordinating frame and in units of pixels. However, because α is a ratio and, thus, remains invariant to frame transforms and units, its value could also be calculated directly in the ultrasound image frame (Fig. 10b), as

$$\alpha = \frac{\|{}^{U}X_1 - {}^{U}X_2\|}{\|{}^{U}X_1 - {}^{U}X_3\|} \tag{6}$$

Combining eqn 5 and eqn 6 yields

$${}^{H}X_2 = {}^{H}A + \frac{\|{}^{U}X_1 - {}^{U}X_2\|}{\|{}^{U}X_1 - {}^{U}X_3\|} \cdot \left({}^{H}D - {}^{H}A\right) \tag{7}$$

where ${}^{H}A$ and ${}^{H}D$ were measurable from the *Double-N* phantom geometry, while ${}^{U}X_1$, ${}^{U}X_2$ and ${}^{U}X_3$ were automatically extracted by the segmentation algorithm. As a result, we were able to calculate ${}^{H}X$ directly from ${}^{U}X$ in the acquired ultrasound images of the phantom.

The aforementioned shows how we found one ${}^{H}X$ position using one set of N-wires. In theory, the more points we collected for the least-mean-squares method to solve for ${}^{P}_{U}T$ in eqn 3, the more accurate the calibration outcome would be. In practice, we acquired two sets of N-wires of the *Double-N* phantom in a single image, using multiple freehand images. Note that α is unique for individual N-wire, so eqn 7 needed to be evaluated for each set of N-wires to yield a corresponding ${}^{H}X$. Due to the fast, automatic segmentation algorithm, all process could be done in real time.

Measuring the Double-N *phantom geometry.* We employed a precalibrated Stylus probe (HP005 Integrated, Traxtal Inc., Toronto, ON, Canada) to measure the phantom geometry. First, we probed a set of physical landmarks on the *Double-N* phantom that were precisely machined with a known geometry; then, we registered this geometry to the optical target that was affixed to the phantom, by which the phantom coordinate frame was defined. The entire probing process was guided by an interactive graphics interface provided to the user and required a few seconds to accomplish.

A general form to solve for the calibration parameters. Generally, if we use the form, ${}^{H}X\,(r_i, c_i^1, c_i^2)$, to represent the i^{th} point in the phantom frame that we have collected from the N-shape at row r and between columns c^1 and c^2; and ${}^{U}X\ (r_i, c_i^1, c_i^2)$, the corresponding point in the ultrasound image frame, and with α_i calculated from eqn 6, we could rewrite eqn 7 as:

$$ {}^{H}X\big(r_i, c_i^1, c_i^2\big) = A\big(r_i, c_i^1\big) + \alpha_i \cdot \big(D\big(r_i, c_i^2\big) - A\big(r_i, c_i^1\big)\big) \quad (8) $$

Equation 3 could then be rewritten in a general form

$$ {}^{P}_{U}T \cdot {}^{U}X\big(r_i, c_i^1, c_i^2\big) = {}^{P}_{T}T \cdot {}^{T}_{D}T \cdot {}^{D}_{H}T \cdot {}^{H}X\big(r_i, c_i^1, c_i^2\big) \qquad (9) $$

Bear in mind that both ${}^{U}X\ (r_i, c_i^1, c_i^2)$ and ${}^{H}X\ (r_i, c_i^1, c_i^2)$ are 4×1 column vectors in homogeneous format, so eqn 9 would be particularly useful for implementation because we can construct ${}^{U}X = [{}^{U}x\ {}^{U}y\ 0\ 1]^T$ and ${}^{H}X = [{}^{H}x\ {}^{H}y\ {}^{H}z\ 1]^T$ in matrices using ${}^{U}X\ (r_i, c_i^1, c_i^2)$ and ${}^{H}X\ (r_i, c_i^1, c_i^2)$ as their respective column vectors:

$$ {}^{U}X = \big({}^{U}X\big(r_0, c_0^1, c_0^2\big), {}^{U}X\big(r_1, c_1^1, c_1^2\big), \cdots, {}^{U}X\big(r_i, c_i^1, c_i^2\big), \cdots\big) = \begin{pmatrix} {}^{U}x_0 & {}^{U}x_1 & \cdots & {}^{U}x_i & \cdots & {}^{U}x_N \\ {}^{U}y_0 & {}^{U}y_1 & \cdots & {}^{U}y_i & \cdots & {}^{U}y_N \\ 0 & 0 & \cdots & 0 & \cdots & 0 \\ 1 & 1 & \cdots & 1 & \cdots & 1 \end{pmatrix} \qquad (10) $$

and

$$ {}^{H}X = \big({}^{H}X\big(r_0, c_0^1, c_0^2\big), {}^{H}X\big(r_1, c_1^1, c_1^2\big), \cdots, {}^{H}X\big(r_i, c_i^1, c_i^2\big), \cdots\big) = \begin{pmatrix} {}^{H}x_0 & {}^{H}x_1 & \cdots & {}^{H}x_i & \cdots & {}^{H}x_N \\ {}^{H}y_0 & {}^{H}y_1 & \cdots & {}^{H}y_i & \cdots & {}^{H}y_N \\ {}^{H}z_0 & {}^{H}z_1 & \cdots & {}^{H}z_i & \cdots & {}^{H}z_N \\ 1 & 1 & \cdots & 1 & \cdots & 1 \end{pmatrix} \qquad (11) $$

Note the difference in the third rows between matrices of ${}^{U}X$ and ${}^{H}X$. Points in the US image frame do not have a z-coordinate, so without losing generality we use all zeros for their third components.

In all, what eqns 9, 10 and 11 have established is an overdetermined system for ${}^{P}_{U}T$, which can be solved using a straightforward implementation of least mean squares.

Automatic accuracy feedback and control

Automatic evaluation on the calibration accuracy. Direct evaluation of calibration accuracy can be challenging because of the lack of a reliable way to obtain the exact spatial relationship between the ultrasound image plane and the probe. A common work-around is to measure how closely a 3D reconstructed position derived from a ultrasound image (after applying the calibration parameters) is to its true physical location (*i.e.,* to ground truth (Mercier et al. 2005)). The same principle can be extended to more complex structures, *e.g.,* to scan a specially designed phantom (Lindseth et al. 2003) or, even simpler, the calibration phantom itself (Pagoulatos et al. 2001).

Similar to the approach of Pagoulatos et al (2001), we employed the *Double-N* phantom to test our calibration accuracy. We were able to fully automate the error evaluation in real time by iteratively reconstructing the N-wire positions in the physical phantom space using the current calibration results and, then, compared them with a ground truth - the known wire locations from the *Double-N* phantom geometry - as

$$ \|FRE\| = \|{}^{H}X - {}^{H}_{T}T \cdot {}^{H}_{T}T \cdot {}^{P}_{U}T \cdot {}^{U}X\| \qquad (12) $$

where ${}^{P}_{U}T$ was the current calibration result to validate, ${}^{H}_{T}T$ and ${}^{T}_{P}T$ were known by the optical targets affixed on *Double-N* phantom and the ultrasound probe, and ${}^{H}X$ and ${}^{U}X$, the identified positions in the respective phantom and ultrasound image space. This is commonly referred to as "fiducial registration error (FRE)" (Mercier et al. 2005) because it shares the same principle as the use of fiducials in known positions to judge a registration error only that, instead of point fiducials, line fiducials from the construction of N-wires were used here. Because $\|FRE\|$ is an absolute distance between two positions in space, it remains invariant to frame transformations. Hence, for easier visualization of the error distributions, we converted the FRE from the phantom space (H) to the physical transducer frame defined with respect to the alignment of crystal arrays (C) as in Fig. 11a, by series of rigid frame transformations:

$$ {}^{C}FRE = {}^{C}_{P}T \cdot {}^{P}_{T}T \cdot {}^{T}_{H}T \cdot {}^{H}FRE \qquad (13) $$

where ${}^{C}_{P}T$ is constructed using ${}^{T}_{P}T$ but with unit scaling (so that the units of FRE remains in meters). Two things are important to note about our real-time error evaluation:

- Because the same phantom geometry was utilized for both calibration and validation, we separated the data used for validation from that of calibration to avoid the systematic bias in error evaluation toward the calibration results. Our calibration system acquired a fresh set of input data from the *Double-N* phantom before the calibration started and reserved this data set for validation purposes only.
- One significant advantage of the automatic error retrieval is that the accuracy evaluation could be conducted quickly and efficiently for an extensive data set collected from a great number of experimental conditions to thoroughly investigate and validate the calibration system. We tested our calibration system extensively through a large data set of 10,000 freehand images and did so in a very short period of time, which would not be possible for the conventional two-phase manual validation procedures.

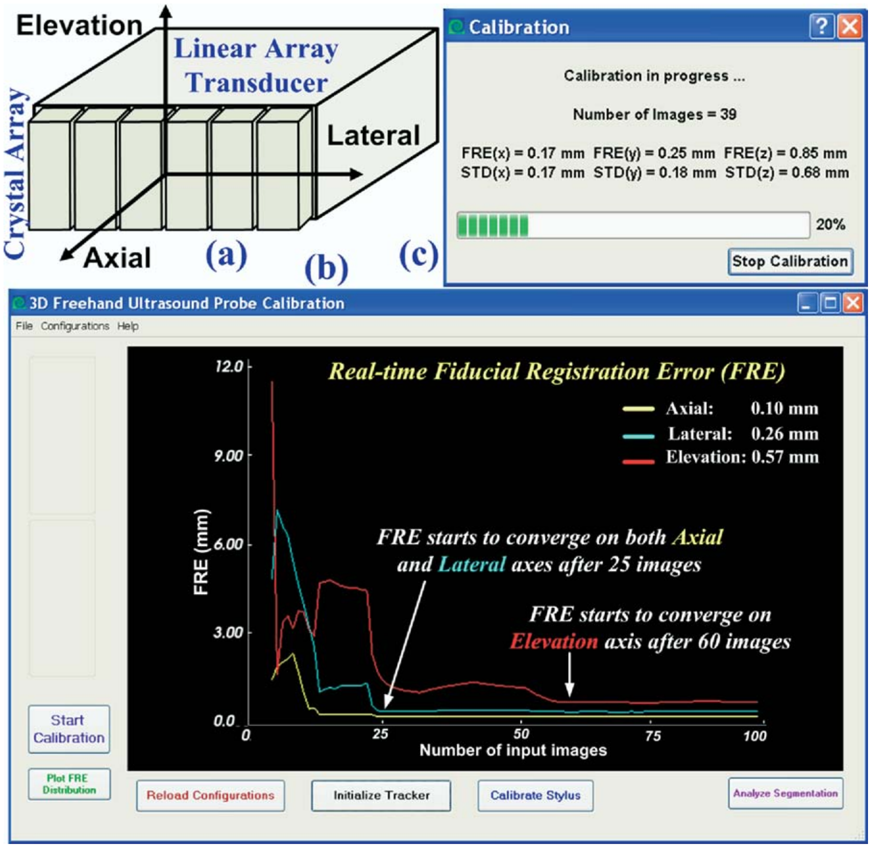

Fig. 11. Real-time calibration accuracy feedback and control. (a) The definition of the physical transducer frame with respect to the crystal alignments, in *axial, lateral* and *elevation* axes; (b) The graphical user interface of the calibration system displaying in real time the fiducial registration error (FRE) converging curves with respect to the number of input images, along the axial, lateral and elevation axes, respectively; (c) The dialogue interface provided to the user to terminate the calibration process and output the current calibration results if the FRE starts to converge or falls below a satisfactory threshold.

Real-time update, feedback and control of FREs. FREs were updated and displayed in real time to the user via a graphical interface (Fig. 11b). There were three pieces of critical information conveyed to the user during the calibration:

1. The vertical axis was the FRE value, calculated on-the-fly during each iteration, and the horizontal axis showed the number of input images used to estimate these calibration parameters. We expected to see that with more and more input images, the calibration error becomes smaller and smaller (which is clear in this example).
2. Three color-coded curves were displayed, each representing the FRE components along the axial, lateral and elevation axes. This gave the user a visual inspection of how the error was distributed along these three directions. In the example illustrated, it can be seen that the elevational component of FRE (the red curve) had larger values and greater dynamics than the other two components. Also, errors in the elevation axis dominated the overall calibration error.
3. With fewer input images initially, the FRE curves fluctuated significantly at the beginning but eventually smoothed down to a stable state as more data was acquired. This showed the converging pattern of the FREs as the number of input images increased. In the example illustrated, both axial and lateral components of the FRE started to converge after around 25 input images but it took 60 images for convergence in the elevation axis. In general, when all the FRE curves started to converge, it was usually a good indication that the calibration error had reached a stable minimum and the user could stop the calibration.

After all FRE curves either converged or fell below a desired threshold, the calibration system provided an interactive interface (Fig. 11c) for the user to terminate the process and output the final calibration result.

Table 1. Variance in the segmentation outcome: automatic system vs. human operators

Variance (in pixels)	Automatic		Human	
	Mean	Max	Mean	Max
Axial	0.00	0.00	0.46	0.80
Lateral	0.00	0.00	0.64	1.10

RESULTS

Extensive tests were conducted to evaluate the accuracy, precision, and performance of the segmentation method and the overall calibration process.

Part one. Segmentation accuracy, precision and robustness

Validation of segmentation accuracy. For a test of accuracy, we randomly selected 100 images acquired from the *Double-N* phantom and visually inspected them for the locations of the six N-fiducials. This gave us a total of 600 independent measurements as the ground truth to compare with the results suggested by the automatic segmentation. The algorithm correctly identified all 600 N-fiducials positions (100% recognition rate). More importantly, the results were precise to one tenth of a pixel, whereas manual segmentation had a precision of only one pixel.

Segmentation precision: Automatic vs. human. We compared the precision of the automatic algorithm with that of human operators by evaluating the variance in segmentation outcomes. A set of distinct ultrasound images (acquired freehand from the *Double-N* phantom at various image depths and with varying image quality) were provided to seven volunteer subjects for manual extraction of the N-fiducials: every image was segmented 10 times by each subject to obtain the variances in the manual process. The subjects were selected such that their level of expertise in segmenting ultrasound image varies from low to high: two were new students with zero or minimal expertise to the task, three were graduate students with moderate expertise and one graduate student and one post-doctoral fellow had years of experience in ultrasound segmentation and did segmentation on a regular basis. We then performed the same procedure on the automatic algorithm. The results are shown in Table 1

As expected, the automatic algorithm was deterministic and had zero variance in its output. The human segmentations, on the other hand, had large variances for all subjects. Variances were larger in the lateral direction, an unsurprising result given the poorer (than axial) lateral resolution. Variances were also greater for the less experienced subjects, also unsurprising; the individual variances are shown in Fig. 12.

Segmentation performance and speed

Aside from being able to accurately and robustly extract the N-fiducials, the segmentation algorithm was fast and ran in real time. Implemented in C++ and without hardware or software optimization, it only took the algorithm on average 0.17 s to segment a single image.

Part Two. Calibration accuracy, robustness and performance

One advantage of our fast segmentation algorithm was that it enabled us to easily validate the calibration system on a large set of ultrasound images acquired under various experimental conditions.

- We tested the calibration system on a set of 10,000 images, acquired from the *Double-N* phantom in freehand motion. The images were captured from a wide range of angles and depths that the ultrasound probe could be physically placed within the phantom.

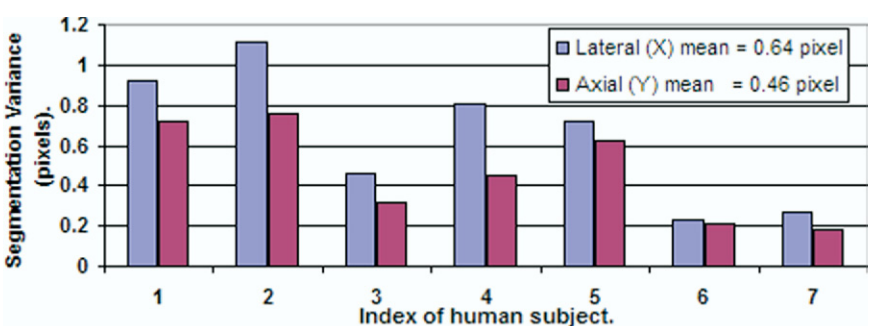

Fig. 12. Variance in manual segmentation for seven human subjects. Subjects 1 and 2 were new students; subjects 3 through 5 were senior graduate students with moderate expertise; subject 6 was a senior graduate student expert in the task; and subject 7 was a post-doctoral fellow expert in the task.

Table 2. FRE for 50 independent calibration trials

	Fiducial registration error (mm)			
Number of trials 50	Axial	Lateral	Elevation	Norm
Mean (μ)	0.14	0.19	0.62	0.66
Standard deviation (σ)	0.12	0.22	0.64	-
Minimum (best case)	0.05	0.10	0.34	0.36
Maximum (worst case)	0.29	0.33	1.02	1.11

- Data were randomly divided into 50 groups of 200 images in each. This established 50 independent trials for testing. To avoid bias, the data for validation were separated from those of calibration.
- For validation, we estimated the FRE from the first 80 images in each group of data, computing the means and standard deviations per group.
- For calibration, images were taken from the other 120 images in each group of data and then fed to the calibration system to calculate the calibration parameters.

Calibration accuracy and robustness. Table 2 summarizes the validation results of our calibration system, including the mean and the standard deviation of FREs of the 50 independent random trials, as well as the best and worst cases among all trials. For comparison, all results were illustrated along the axial, lateral and elevation axes, respectively. Observations on the calibration system's accuracy and robustness include:

(1) The FRE on average were 0.14 $\pm$ 0.12 mm, 0.19 $\pm$ 0.22 mm and 0.62 $\pm$ 0.64 mm, along the axial, lateral and elevation axes, respectively. Overall, in 49 out of the 50 independent experiments, the FRE converged to sub-millimeter in all of the axial, lateral and elevation axes and five yielded a FRE in excess of 0.9 mm; there was only one trial had a maximum observed FRE slightly exceeding 1 mm (1.02 mm in the elevational direction). This indicates the calibration system was able to consistently achieve submillimeter accuracy in 98% of cases.

(2) The mean of 3D FRE (measured in Euclidian distance) of all 50 independent trials was 0.66 mm, which is consistent with accuracy reported by related work with N-wire phantoms (Pagoulatos et al. 2001; Zhang et al. 2004; Hsu et al. 2007).

(3) The elevation axis had a much larger FRE mean and standard deviation (more than three times larger) than that of the axial and lateral directions. On the other hand, the errors and variances were always the smallest along the axial direction.

The obvious differences of FRE distributions among the axial, lateral and elevation axes were the clear evidences of how the ultrasound resolution varies *axially, laterally,* and *elevationally:*

(a) As discussed above, the axial resolution (around 0.1 mm for the transducer at the frequency we used) was much finer than the lateral resolution, resulting in less uncertainty and error axially than laterally.

(b) The ultrasound elevation resolution was the dominant influence on calibration accuracy. Similar to the lateral direction, the ultrasound beam had a finite beam width in the elevation axis, referred to as section thickness (Goldstein and Madrazo, 1981), which determined the elevation resolution. Unlike the lateral axis, there were no multiple crystals in the out-of-plane direction to provide electronic focusing. The beam was therefore only focused mechanically in the elevation axis, by either curving the crystal or placing an acoustic lens in front (Hedrick et al. 2005). This resulted in a much larger elevation beam width, which contributed to the larger uncertainties and errors among all axes.

Calibration system performance. The calibration system was also reasonably fast. Each of the 50 trials converged in an average of 12.5 s, sufficiently fast for many applications in an operating room.

DISCUSSION

The design of the *Double-N* phantom facilitated fast, accurate calibration with minimal operator interaction. The system required more images than did related reported techniques and the phantom design could be improved. One notable limitation is the lack of temporal calibration.

To converge, our system always required fewer than 60 images with an average of 2 data points (2 sets of N-wires) each, compared with 30 images with an average of four N-wire sets per image (Pagoulatos et al. 2001; Zhang et al. 2004; Chen et al. 2005) or six images with an average of 19 N-wire sets per image (Hsu et al. 2007). In this work and related work, we observe that the key value seems to be 120 data points - this is the minimum reported number for high-accuracy calibration. Other phantom designs have provided more data per image but at the cost of complexity and requiring human interaction in the image-segmentation stage. We have traded off the number of images needed (more) against human interaction (zero) and phantom complexity (minimum).

The calibration phantom described here was a preliminary design and can be improved upon. We found the phantom to be small, limiting freehand motion. The design was optimized for our higher-frequency ultrasound probes and is not suitable for low frequencies.

The phantom was inspected by a local hospital's biomedical engineering group and deemed suitable for intra-operative use. The phantom, including the dynamic reference, was successfully sterilized using a low-temperature plasma of hydrogen peroxide. In one test, some of the nylon wires failed by melting. Future versions of the phantom may use different material for the wires or may be constructed for easy assembly in the operating room. A simple solution, for example, would be to use surgical clips instead of silicon glue to affix the wires and to adjust the wire tensions.

A minor technical limitation of our system is that we did not perform temporal calibration., *i.e.,* we did not tightly synchronize the tracking with the image capture (Mercier et al. 2005). Although the effect of temporal calibration would be minimal if the probe motion is relatively slow, this is a straightforward potential improvement for a future generation of our design.

CONCLUSIONS

We have presented a real-time freehand ultrasound calibration system with automatic accuracy control, including several features crucial for intraoperative surgical use:

(1) a calibration phantom that facilitates the same level of calibration accuracy as that of conventional N-wire phantoms, with a simple, low-maintenance and sterilizable design;
(2) a fully automatic segmentation and calibration algorithm that requires no human interaction beyond acquiring the ultrasound images; and
(3) an automatic error computation and control method to ensure calibration accuracy.

Experiments were conducted on a data set of 10,000 images to thoroughly investigate and validate the accuracy, robustness and performance of the calibration system. The results demonstrated that the calibration system was able to consistently and robustly achieve very high accuracy with real-time efficiency. Work is currently underway to thoroughly verify the performance of the system under actual operating-room conditions.

Acknowledgments—This research was supported in part by the Canada Foundation for Innovation, the Canadian Institutes of Health Research, the Ontario Research and Development Challenge Fund and the Natural Sciences and Engineering Research Council of Canada.

REFERENCES

Barratt DC, Penney GP, Chan CSK, et al. Self-calibrating 3D-ultrasound-based bone registration for minimally invasive orthopedic surgery. IEEE Trans Med Imaging 2006;25:312–323.
Barry CD, Allott CP, John NW, et al. 3D freehand ultrasound: Image reconstruction and volume analysis. Ultrasound Med Biol 1997;23:1209–1224.
Boctor EM, Iordachita I, Fichtinger G, Hager GD. Real-time quality control of tracked ultrasound. Lecture Notes in Computer Science 2005;3749:621–630.
Boctor EM, Iordachita I, Choti MA, Hager G, Fichtinger G. Bootstrapped ultrasound calibration. Stud Health Technol Inform 2006a;119:61–66.
Boctor EM, Iordachita I, Fichtinger G, Hager GD. Ultrasound self-calibration. In: Cleary KR, Galloway RL Jr. eds, Proceedings of SPIE Medical Imaging: Visualization, Image-Guided Procedures, and Display. San Diego, CA, SPIE Press. USA: 2006b;6141:61412N1–61412N12.
Boctor EM, Jain A, Choti MA, Taylor RH, Fichtinger G. Rapid calibration method for registration and 3D tracking of ultrasound images using spatial localizer. In: Walker WF, Insana MF, eds. Proceedings of SPIE Medical Imaging: Ultrasonic Imaging and Signal Processing. SPIE, San Diego, CA, SPIE Press. USA: 2003;5035:521–532.
Booch G, Jacobson I, Rumbaugh J. Unified Modeling Language User Guide, The Addison-Wesley Object Technology Series. Addison-Wesley Professional. 1998.
Brown RA. A stereotactic head frame for use with ct body scanners. Invest Radiol 1979;14:300–304.
Chen TK. A system for ultrasound-guided computer-assisted orthopaedic surgery. Master's thesis, Queen's University, Kingston, Ontario, Canada, January 2005.
Chen TK, Abolmaesumi P, Pichora DR, Ellis RE. A system for ultrasound-guided computer-assisted orthopaedic surgery. Comput Aided Surg 2005;10:281–292.
Comeau RM, Fenster A, Peters TM. Integrated mr and ultrasound imaging for improved image guidance in neurosurgery. In: Hanson KM ed. Proceedings of SPIE Medical Imaging: Image Processing. San Diego, CA, SPIE Press. USA: 1998;3338:747–754.
Eggert DW, Lorusso A, Fisher RB. Estimating 3D rigid body transformations: a comparison of four major algorithms. Mach Vision Appl 1997;9:272–290.
Goldstein A, Madrazo BL. Slice-thickness artifacts in gray-scale ultrasound. Clin Ultrasound 1981;9:365–375.
Gonzalez R, Woods, R. Digital image processing. 2nd edition. Upper Saddle River, NJ: Prentice-Hall, Inc., USA. 2002.
Hedrick WR, Hykes DL, Starchman DE. Ultrasound physics and instrumentation, 4th edition. Missouri: Elsevier Mosby, 2005.
Hsu PW, Prager RW, Gee AH, Treece GM. Real-time freehand 3D ultrasound calibration. In: Emelianov SY, McAleavey SA eds, Proceedings of SPIE Medical Imaging: Ultrasonic Imaging and Signal Processing. San Diego, CA, SPIE Press. USA. 2007;6513:6513081–6513088.
Kremkau FW. Diagnostic ultrasound: Principles and instruments, 6th ed. Philadelphia: W.B. Saunders Company, 2002.
Lindseth F, Tangen GA, Lango T, Bang J. Probe calibration for freehand 3D ultrasound. Ultrasound Med Biol 2003;29:1607–1623.
Mercier L, Lang∅ T, Lindseth F, Collins LD. A review of calibration techniques for freehand 3D ultrasound systems. Ultrasound Med Biol 2005;31:449–471.
Muratore DM, Galloway Jr. RL. Beam calibration without a phantom for creating a 3D freehand ultrasound system. Ultrasound Med Biol 2001;27:1557–1566.
Northern Digital Inc., Optotrak Certus Specifications. NDI P/N 8300176. July 2004.
Pagoulatos N, Haynor DR, Kim Y. Fast calibration for 3D ultrasound imaging and multimodality image registration. In: Proceedings of the First Joint BMES/EMBS Conference. Atlanta, GA, IEEE Press. USA: 1999;2:1065–1065.
Pagoulatos N, Haynor DR, Kim Y. A fast calibration method for 3D tracking of ultrasound images using a spatial localizer. Ultrasound Med Biol 2001;27:1219–1229.
Prager RW, Rohling RN, Gee AH, Berman L. Rapid calibration for 3D freehand ultrasound. Ultrasound Med Biol 1998;24:855–869.
Sciavicco L, Siciliano B. Modelling and control of robot manipulators, 2nd ed. New York, NY: Springer Publishing Company, USA. 2000.
Zhang WY, Rohling RN, Pai DK. Surface extraction with a 3D freehand ultrasound system. Ultrasound Med Biol 2004;30:1461–1473.